Numerical Quadrature of the Subband Distribution Functions in Strained Silicon UTB Devices

Oskar Baumgartner, Markus Karner, Viktor Sverdlov, and Hans Kosina
Institute for Microelectronics, TU Wien, Gußhausstraße 27–29, A–1040 Wien, Austria
Email: {baumgartner|karner|sverdlov|kosina}@iue.tuwien.ac.at

***Abstract*—In this work, the $\mathbf{k}\cdot\mathbf{p}$ method is used to calculate the electronic subband structure. To reduce the computational cost of the carrier concentration calculation and henceforth the required number of numerical solutions of the Schrödinger equation, an efficient 2D k-space integration by means of the Clenshaw-Curtis method is proposed. The suitability of our approach is demonstrated by simulation results of Si UTB double gate nMOS and pMOS devices.**

I. Introduction

Strained silicon ultra-thin body MOSFETs are considered to be good candidates for CMOS integration in the post 22 nm technology nodes. An accurate description of such devices relies on the modeling of the subband structure. An efficient self-consistent Schrödinger-Poisson model for the calculation of the electronic subband structure is presented, taking into account band nonparabolicity and arbitrary strain [1]. A two-band $\mathbf{k}\cdot\mathbf{p}$ Hamiltonian has been used for electrons and a six-band $\mathbf{k}\cdot\mathbf{p}$ Hamiltonian for holes.

II. Calculation of the Subband Structure

The numerical modeling of the subband structure in ultra thin body SOI MOS structures relies on an accurate model of the bulk Hamiltonian. We applied a two-band $\mathbf{k}\cdot\mathbf{p}$ Hamiltonian [2], [3] to describe the silicon conduction band around the X points.

$$\mathbf{H}=\begin{bmatrix}\mathrm{H}_- & \mathrm{H}_{\mathrm{bc}}\\ \mathrm{H}_{\mathrm{bc}} & \mathrm{H}_+\end{bmatrix}\qquad\text{with}$$

$$\mathrm{H}_\mp=\mathcal{E}_{\mathrm{c}}(z)+\frac{\hbar^2k_{\mathrm{z}}^2}{2m_{\mathrm{l}}}+\frac{\hbar^2\left(k_{\mathrm{x}}^2+k_{\mathrm{y}}^2\right)}{2m_{\mathrm{t}}}\mp\frac{\hbar^2k_0k_{\mathrm{z}}}{m_{\mathrm{l}}},$$

$$\mathrm{H}_{\mathrm{bc}}=D\epsilon_{\mathrm{xy}}-\frac{\hbar^2k_{\mathrm{x}}k_{\mathrm{y}}}{M}.$$

$\mathcal{E}_{\mathrm{c}}$ denotes the conduction band edge energy, m_{l} and m_{t} are the longitudinal and transversal electron masses, respectively, and $\frac{1}{M}\approx\frac{1}{m_{\mathrm{t}}}-\frac{1}{m_{\mathrm{e}}}$. The shear strain deformation potential $\mathrm{D}=14\mathrm{eV}$ and the off-diagonal strain component ϵ_{xy} describe the effects of shear strain on the bandstructure. $k_0=0.15\frac{2\pi}{a_0}$ corresponds to the distance of the valley to the X point.

To model the silicon valence band structure a $6\times6-\mathbf{k}\cdot\mathbf{p}$ Hamiltonian [4] has been implemented. Following the notation of Manku it is written as

$$\mathbf{H}=\mathcal{E}_{\mathrm{v}}\mathbf{I}_{6\times6}+\begin{bmatrix}\mathbf{S}+\mathbf{D} & \mathbf{0}_{3\times3}\\ \mathbf{0}_{3\times3} & \mathbf{S}+\mathbf{D}\end{bmatrix}+\mathbf{H}_{\mathbf{so}},$$

where $\mathcal{E}_{\mathrm{v}}$ is the valence band edge and the perturbation matrix $\mathbf{S}$ and the deformation potential matrix $\mathbf{D}$ are given by

$$\mathbf{S}=\begin{bmatrix}Lk_{\mathrm{x}}^2+M(k_{\mathrm{y}}^2+k_{\mathrm{z}}^2) & Nk_{\mathrm{x}}k_{\mathrm{y}} & Nk_{\mathrm{x}}k_{\mathrm{z}}\\ Nk_{\mathrm{x}}k_{\mathrm{y}} & Lk_{\mathrm{y}}^2+M(k_{\mathrm{x}}^2+k_{\mathrm{z}}^2) & Nk_{\mathrm{y}}k_{\mathrm{z}}\\ Nk_{\mathrm{x}}k_{\mathrm{z}} & Nk_{\mathrm{y}}k_{\mathrm{z}} & Lk_{\mathrm{z}}^2+M(k_{\mathrm{x}}^2+k_{\mathrm{y}}^2)\end{bmatrix}$$

$$\mathbf{D}=\begin{bmatrix}l\varepsilon_{\mathrm{xx}}+m(\varepsilon_{\mathrm{yy}}+\varepsilon_{\mathrm{zz}}) & n\varepsilon_{\mathrm{xy}} & n\varepsilon_{\mathrm{xz}}\\ n\varepsilon_{\mathrm{xy}} & l\varepsilon_{\mathrm{yy}}+m(\varepsilon_{\mathrm{xx}}+\varepsilon_{\mathrm{zz}}) & n\varepsilon_{\mathrm{yz}}\\ n\varepsilon_{\mathrm{xz}} & n\varepsilon_{\mathrm{yz}} & l\varepsilon_{\mathrm{zz}}+m(\varepsilon_{\mathrm{xx}}+\varepsilon_{\mathrm{yy}})\end{bmatrix}$$

As parameters for the silicon valence band structure without strain $L=-6.53$, $M=-4.64$, and $N=-8.75$ in units of $\frac{\hbar^2}{2m_{\mathrm{e}}}$ have been used [5]. l, m, and n are the strain deformation potentials for the valence band.

The spin orbit coupling is described by the Hamiltonian

$$\mathbf{H}_{\mathbf{so}}=-\frac{\mathcal{E}_{\mathrm{so}}}{3}\begin{bmatrix}0 & \mathrm{i} & 0 & 0 & 0 & -1\\ -\mathrm{i} & 0 & 0 & 0 & 0 & \mathrm{i}\\ 0 & 0 & 0 & 1 & -\mathrm{i} & 0\\ 0 & 0 & 1 & 0 & -\mathrm{i} & 0\\ 0 & 0 & \mathrm{i} & \mathrm{i} & 0 & 0\\ -1 & -\mathrm{i} & 0 & 0 & 0 & 0\end{bmatrix},$$

with the split off energy of silicon $\mathcal{E}_{\mathrm{so}}=44\,\mathrm{meV}$.

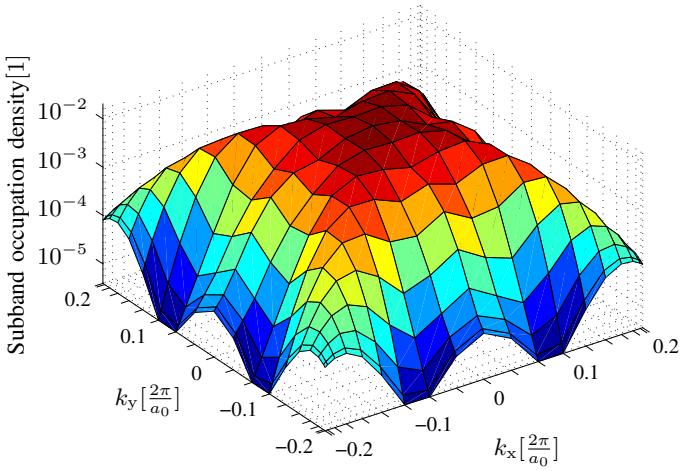

Fig. 1. Occupation of the heavy hole band of Si in a 3 nm wide quantum well. The grid shows the nodes of the numerical quadrature.

978-1-4244-3927-0/09/$25.00 ©2009 IEEE

Quantization is introduced in the bulk Hamiltonian by the substitution $k_z \rightarrow -\mathrm{i}\,\partial_z$, where the z-axis is the quantization direction and corresponds to the normal of the (001) silicon crystal surface throughout this work. A finite difference scheme with hard wall boundary conditions has been used to discretize the Schrödinger equation. The resulting eigenvalue problem gives rise to discrete energies describing the subband structure.

III. Numerical Quadrature of the Subband Distribution Functions

The contribution of subband i and valley j to the equilibrium electron concentration is given by

$$n_{i,j}(z) = \int_{\mathrm{BZ}} \mathrm{d}^2\mathbf{k}\,|\psi_{i,j}(z)|^2\,\frac{1}{(2\pi)^2} f_0\left(\mathcal{E}_{i,j}\left(k_\mathrm{x},k_\mathrm{y}\right)-\mathcal{E}_\mathrm{F}\right),$$

where $\psi_{i,j}$ is the wave function and f_0 is the Fermi distribution and $\mathcal{E}_\mathrm{F}$ the Fermi level with a similar relationship holding for the hole concentration in a pMOS device. Therefore, to calculate the occupation of a subband a numerical, two-dimensional $\mathbf{k}$-space integration is required. This necessitates to solve the Schrödinger equation for every discrete point $(k_\mathrm{x},k_\mathrm{y})$. Hence, one seeks after a numerical quadrature scheme that gives good accuracy on a coarse grid. In contrast to previous work [6] which made use of harmonic and cubic spline interpolation for $\mathbf{k}$-space integration, in this work the Clenshaw-Curtis method [7] has been applied. As nodes in the integration interval $[-1,1]$ the zeros of the Chebyshev polynomial are used: $x_k := \cos(k\frac{\pi}{N})$ with $k = 0,1,\ldots,N$. Following [8], the weights are written explicitly as

$$w_k = \frac{c_k}{N}\left(1-\sum_{j=1}^{\lfloor N/2\rfloor}\frac{b_j}{4j^2-1}\cos\left(2jk\tfrac{\pi}{N}\right)\right)$$

with $b_j = 1$ if $j = N/2$, or $b_j = 2$, if $j < N/2$, and $c_k = 1$ if $k \mod N = 0$, or $c_k = 2$ otherwise. For the $\mathbf{k}$-space integration of the subbands provided by the $\mathbf{k}\cdot\mathbf{p}$ Hamiltonian excellent accuracy has been achieved with only 19 nodes per k direction.

IV. Results and Discussion

A (001) silicon UTB DG-MOSFET with 3 nm film and 1 nm oxide thickness has been simulated. For the nMOS device the donor doping of the polysilicon gates was $\mathrm{N_D} = 1.0\times10^{20}\,\mathrm{cm}^{-3}$ and the Si film was lightly p-doped at $\mathrm{N_A} = 2.0\times10^{16}\,\mathrm{cm}^{-3}$, while the complementary doping has been used for the pMOS device. The occupation function of the heavy hole band is depicted in Fig. 1. Equivalently the lowest unprimed subband of the nMOS device with and without shear strain is depicted in Fig. 2. The grid as shown in the figures corresponds to the nodes of the Clenshaw-Curtis quadrature. The zeros of the Chebyshev polynomial give an accumulation of grid points at the boundary of the integration domain. The integration intervals for the nMOS have been chosen as ten percent of the width of the Brillouin zone in each positive and negative direction around the valley. For the pMOS device the boundaries have been set at $k_{\mathrm{x,y}} = \pm0.2\frac{2\pi}{a_0}$. Therefore, the domain has to be normalized accordingly to the interval $[-1,1]$ of the Clenshaw-Curtis rule.

Fig. 3 shows the self-consistent conduction band edge and the electron concentration for the nMOS and Fig. 4 the corresponding result for the pMOS device. Within the well, the squared wave functions for the four lowest, twofold degenerate unprimed subbands are displayed at their corresponding energy levels. For each subband the electron density is calculated by $\mathbf{k}$-space integration. For the (001) Si-nMOS device the unprimed and primed subband ladder are taken into account to obtain the self-consistent solution.

The convergence behavior of the self-consistent Schrödinger/Poisson loop is shown in Fig. 5. The quadratic norm of the potential update after an iteration evolves similarly for a different number of nodes per k-direction. As depicted in the figure, the convergence behavior is good and hence the iteration scheme proves stable.

To give an impression of the accuracy of the numerical quadrature method a test with parabolic subbands has been

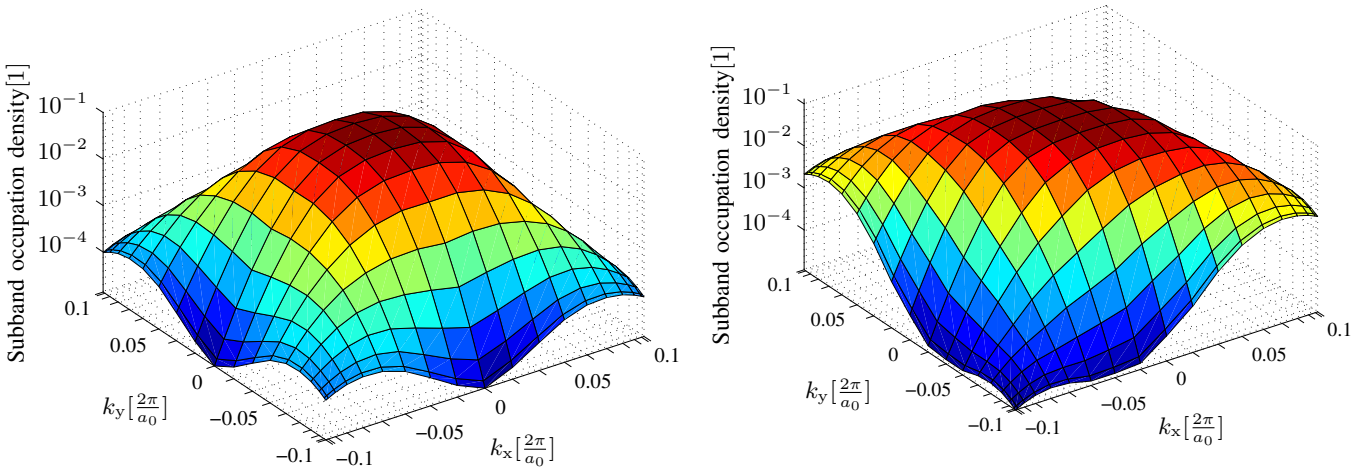

Fig. 2. Occupation of the lowest unprimed subband of a 3 nm (001) silicon conduction band quantum well without strain (left) and with $\varepsilon_{\mathrm{xy}} = 0.5\%$ shear strain (right).

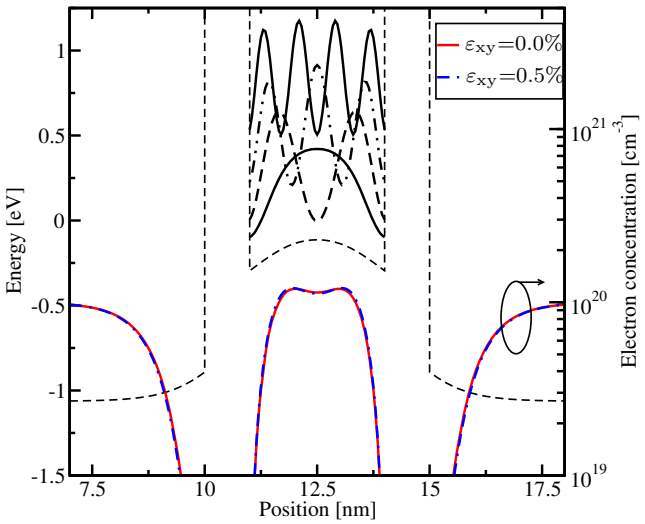

Fig. 3. Self-consistent calculation of the conduction band edge and the electron concentration of a (001) Si-DG-nMOS with 3 nm well width and 1 nm oxide thickness. The normalized wave functions $[\mathrm{nm}^{-1}]$ are overlayed at their respective energy levels. The electron concentration is plotted for the unstrained case and for ε_{xy}=0.5% shear strain.

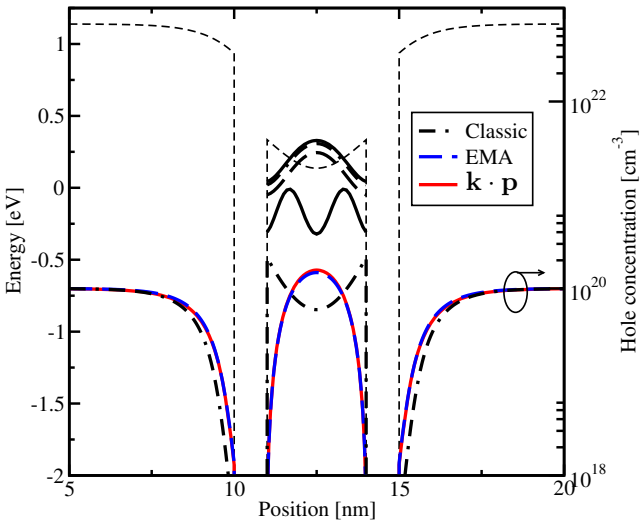

Fig. 4. Same as Fig. 3 but for Si-DG-pMOS device.

conducted. Therefore, a (001) silicon DG-nMOS device has been simulated using the two-band $\mathbf{k}\cdot\mathbf{p}$ Hamiltonian with k_0 and $\frac{1}{M}$ set to zero which corresponds to the parabolic effective mass approximation (EMA). Again, the unprimed and primed valleys are taken into account. This way, the self-consistent carrier concentration has been calculated and compared to the results of the EMA, where the 2D subband density is calculated analytically. The maximum relative difference of the electron concentration for the 3 nm silicon well has been used as measure of accuracy for the numerical quadrature. The results are depicted in Fig. 6. Furthermore, the CPU time for the calculation of the electron concentration on a single core of an Intel Core 2 Quad Q6600 machine is given. This includes the time for solving the Schrödinger equation for all points in $\mathbf{k}$-space and the following numerical quadrature. The curve shows the expected $\mathcal{O}(\mathrm{N}^2)$ behavior of the algorithm.

In Table I the minima of the unprimed (U) and primed (P) subbands are shown in units of eV. The five lowest eigenvalues of the subband ladders are summarized. The eigenvalues of the emulated "parabolic" $\mathbf{k}\cdot\mathbf{p}$ Hamiltonian with k_0 and $\frac{1}{M}$ set to zero and numerically integrated subbands are compared to the energy levels resulting of the effective mass Schrödinger equation. The relative difference of the eigenvalues is given to show the accuracy of the self-consistent result using our proposed calculation scheme.

In Table II the effects of nonparabolicity and strain on the bound states is summed up. As in Table I the unprimed and primed subband ladder is shown in units of eV. The nonparabolic two-band $\mathbf{k}\cdot\mathbf{p}$ Hamiltonian applied to a (001) silicon UTB device gives a two-fold degenerate unprimed valley which is located at the X-point. The four-fold degenerate primed valleys have their minimum at $k = \pm 0.15\frac{2\pi}{a_0}$.

By applying shear strain, the unprimed subbands at the X-point are split and shifted downwards with respect to the primed subband ladder, therefore, favoring the occupation of the unprimed valleys with lower transport mass. Whereas the occupation of the individual subbands is changed fundamentally, the effect on the total electron concentration is marginal

TABLE I

THE MINIMA OF THE UNPRIMED (U) AND PRIMED (P) SUBBANDS ARE SHOWN IN UNITS OF eV. TO TEST THE NUMERICAL QUADRATURE THE TWO-BAND $\mathbf{k}\cdot\mathbf{p}$ HAMILTONIAN HAS BEEN USED WITH k_0 AND $\frac{1}{M}$ SET TO ZERO WHICH CORRESPONDS TO PARABOLIC BANDS. THE RELATIVE DIFFERENCE OF THE EIGENVALUES IS GIVEN TO SHOW THE ACCURACY OF THE SELF-CONSISTENT RESULT USING NUMERICAL INTEGRATION.

EMA		$\mathbf{k}\cdot\mathbf{p}$ parabolic		Relative difference	
U	P	U	P	U	P
−0.11210	0.04745	−0.11214	0.04741	3.6×10^{-4}	8.4×10^{-4}
−0.01494	0.61437	−0.01498	0.61434	2.7×10^{-3}	4.9×10^{-5}
0.19655	1.60525	0.19651	1.60521	2.0×10^{-4}	2.5×10^{-5}
0.49224	2.99374	0.49220	2.99371	8.1×10^{-5}	1.0×10^{-5}
0.87241	4.77407	0.87237	4.77404	4.6×10^{-5}	6.3×10^{-6}

TABLE II

AS IN TABLE I THE UNPRIMED AND PRIMED SUBBAND LADDER IS SHOWN IN UNITS OF eV. BY APPLYING SHEAR STRAIN, THE UNPRIMED SUBBANDS ARE SPLIT AND SHIFTED DOWNWARDS WITH RESPECT TO THE PRIMED LADDER, THEREFORE, FAVORING THE OCCUPATION OF THE UNPRIMED VALLEYS WITH LOWER TRANSPORT MASS.

	$\mathbf{k}\cdot\mathbf{p}$ nonparabolic		$\mathbf{k}\cdot\mathbf{p}$ with $\varepsilon_{xy}=0.5\%$	
	Unprimed	Primed	Unprimed	Primed
1	−0.10148	0.05773	−0.10336	0.07147
	−0.10148		−0.10071	
2	−0.00417	0.62431	−0.02814	0.63826
	−0.00417		0.04673	
3	0.20812	1.61512	0.22144	1.62886
	0.20812		0.23429	
4	0.50491	3.00361	0.51010	3.01732
	0.50491		0.53152	
5	0.88650	4.78393	0.89072	4.79764
	0.88650		0.91224	

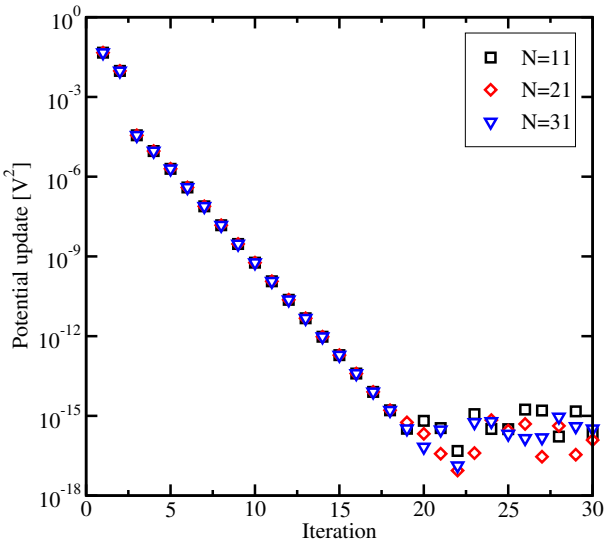

Fig. 5. Potential update after each Schrödinger/Poisson iteration for different numbers of nodes per k-direction of the Clenshaw-Curtis subband integration. Starting from the classical solution all simulations give similar convergence behavior.

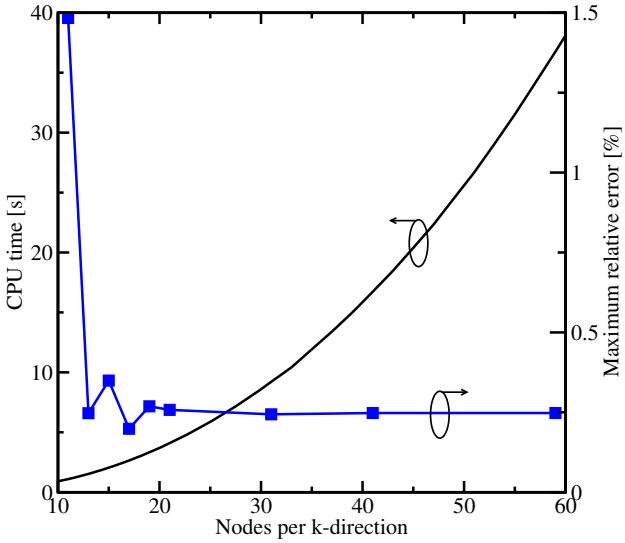

Fig. 6. CPU time for a single Schrödinger/Poisson iteration for different number of nodes per k direction of the Clenshaw-Curtis subband integration. The maximum relative difference of the self-consistent carrier concentration within the well for numerically integrated parabolic subbands with respect to the effective mass approximation with analytically integrated subbands is given to show the good accuracy of the quadrature method.

as shown in Fig. 3.

Similar simulations were carried out for the DG-pMOS device. In the effective mass approximation three types of holes have been considered. The heavy hole band with $m_{\mathrm{hh}} = 0.39m_{\mathrm{e}}$, the light hole band with $m_{\mathrm{lh}} = 0.19m_{\mathrm{e}}$ and the split off band with $m_{\mathrm{so}} = 0.24m_{\mathrm{e}}$ and a shift of 44 meV down from the valence band edge are included in the calculations. As illustrated in Fig. 4 this gives a good agreement of the EMA hole concentration with the self-consistent six-band $\mathbf{k}\cdot\mathbf{p}$ results. The calculated bound states in the UTB are summarized in Table III. Furthermore, compressive stress of 1 GPa in [110] direction was applied. This gives an additional splitting of the heavy hole and light hole band. Under these conditions the transport mass in [110] of the highest band extracted from the $\mathbf{k}\cdot\mathbf{p}$ dispersion relation was $m = 0.17m_{\mathrm{e}}$ as compared to $m = 0.32m_{\mathrm{e}}$ in the unstrained case.

TABLE III
THE BOUND STATES IN A (001) SI DG-PMOS IN UNITS OF EV. FOR THE EFFECTIVE MASS APPROXIMATION THE HEAVY HOLE, LIGHT HOLE AND SPLIT OFF STATES HAVE BEEN CONSIDERED. THE RESULTS ARE COMPARED TO $\mathbf{k}\cdot\mathbf{p}$ SIMULATIONS FOR UNSTRAINED AND STRAINED SI WITH COMPRESSIVE STRESS OF 1 GPA IN [110] DIRECTION.

	EMA			$\mathbf{k}\cdot\mathbf{p}$	
	HH	LH	SO	Unstrained	Strained
1	0.11094	0.00446	0.04758	0.02275	0.04029
2	−0.15444	−0.57724	−0.40559	−0.00009	−0.00842
3	−0.65224	−1.60061	−1.21528	−0.07281	−0.09870
4	−1.34922	−3.03304	−2.34895	−0.36674	−0.34967
5	−2.24353	−4.86962	−3.80274	−0.39456	−0.40065

V. CONCLUSIONS

Contrary to numerical solutions based on the one-band effective mass Schrödinger equation, this work considers a nonparabolic dispersion relation based on a $\mathbf{k}\cdot\mathbf{p}$ Hamiltonian. Furthermore, shear strain effects leading to a warping of the bandstructure are accounted for. The proposed numerical quadrature of the subbands has been successfully applied to electron and hole states in unstrained and strained Si. The self-consistent solutions for the band edges and carrier concentrations of a UTB Si nMOS and pMOS device are presented. The numerical quadrature proves as simple and yet robust method.

ACKNOWLEDGMENT

This work has been supported by the Austrian Science Fund, special research program IR-ON (F2509).

REFERENCES

[1] O. Baumgartner, Markus Karner, Viktor Sverdlov, and Hans Kosina, "Numerical Study of the Electron Subband Structure in Strained Silicon UTB Devices," in *EUROSOI*, 2009, p. 57.

[2] J. C. Hensel, H. Hasegawa, and M. Nakayama, "Cyclotron Resonance in Uniaxially Stressed Silicon. II. Nature of the Covalent Bond," *Phys. Rev.*, vol. 138, no. 1A, pp. A225–A238, April 1965.

[3] E. Ungersböck, S. Dhar, G. Karlowatz, V. Sverdlov, H. Kosina, and S. Selberherr, "The Effect of General Strain on the Band Structure and Electron Mobility of Silicon," *IEEE Transactions on Electron Devices*, vol. 54, no. 9, pp. 2183–2190, 2007.

[4] T. Manku and A. Nathan, "Valence energy-band structure for strained group-IV semiconductors," *J. Appl. Phys.*, vol. 73, no. 3, pp. 1205–1213, February 1993.

[5] F. L. Madarasz, J. E. Lang, and P. M. Hemeger, "Effective masses for nonparabolic bands in p-type silicon," *J. Appl. Phys.*, vol. 52, no. 7, pp. 4646–4648, July 1981.

[6] A.-T. Pham, B. Meinerzhagen, and C. Jungemann, "A fast kp solver for hole inversion layers with an efficient 2D k-space discretization," *J. Comp. Electron.*, vol. 7, no. 3, pp. 99–102, September 2008.

[7] C. W. Clenshaw and A. R. Curtis, "A Method for Numerical Integration on an Automatic Computer," *Num. Math.*, vol. 2, pp. 197–205, 1960.

[8] Jörg Waldvogel, "Fast Construction of the Fejér and Clenshaw-Curtis Quadrature Rules," *BIT*, vol. 46, pp. 195–202, 2006.